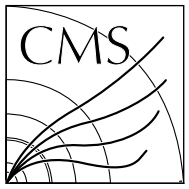

The Compact Muon Solenoid Experiment

CMS Note

Mailing address: CMS CERN, CH-1211 GENEVA 23, Switzerland

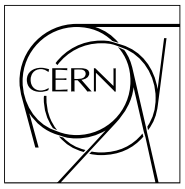

December 10, 2001

Test of CMS Silicon Detector Modules in a 350 MeV/c hadron beam

V. Zhukov[a)]

UIA Antwerpen

T. Bauer, M. Friedl, J. Hrubec, M. Krammer, M. Pernicka

HEPHY Vienna

D. Creanza, V. Radicci

INFN Bari

A. Dierlamm, G. Dirkes, E. Grigoriev, F. Hartmann, S. Heier, F. Röderer

IEKP Universität Karlsruhe (TH)

D. Bisello, A. Kaminsky, G. Marseguerra, D. Pantano, I. Stavitski

INFN Padova

M. Angarano, M. Biasini, G.M.Bilei, S. Cecchetti, L. Fano, M. Giorgi, V. Postolache, L. Servoli

INFN Perugia

Abstract

Several CMS silicon microstrip detectors equipped with APV6 and APV25 readout chips have been exposed to 350 MeV/c pion and proton beams at the Paul Scherrer Institute (PSI, Villigen, CH). We compare the performance of irradiated and non-irradiated silicon sensors as well as the APV6 and APV25 behavior. Various analysis algorithms have been implemented.

[a)] On leave from INP MSU,Moscow

1 Introduction

The Silicon Strip Tracker is an important part of the CMS project at the LHC collider [1].

More than 15000 detector modules provide precision tracking with at least eight hits for each high pt particle. The track reconstruction efficiency depends on the signal-to-noise ratio (SNR) which should exceed eight to assure an efficiency above 98%. Although this SNR is easily achieved for non-irradiated detectors it may significantly degrade while exposing detectors to the equivalent fluence of about $2 \cdot 10^{14}\,\mathrm{n/cm^2}$ expected after 10 years of the LHC operation at the innermost layer of the Silicon Tracker. The irradiation causes an increase of the detector noise and at the same time a decrease of the collection efficiency due to the creation of crystal defects which act as charge traps. Moreover the performance of the front-end readout chip should be considered as well under irradiation.

We have studied the performance of silicon detectors produced by different technologies, irradiated and non-irradiated equipped with APV6 and APV25 (both S0 and S1 versions) readout chips [4] exposed to a 350 MeV/c pion/proton beam at the Paul Scherrer Institute cyclotron facility (PSI). The quasi-continuous pion beam with its 50 MHz structure is very close to the conditions expected in the LHC where bunch crossings occur at 40 MHz.

The measurements were performed in May and December 2000. Thirteen detectors were tested in total, we report the results concerning seven detectors of different types here.

2 Detector modules

2.1 Sensors

The sensor specifications are summarized in table 1.

Table 1:

detector	sensors	specification (p,l,crystal,ρ,O)	n(1MeV)/cm^2	readout
PD26	2 × Micron	61 μm, 12 cm, $<100>$ 2 kΩ cm, OX	-	1 × APV25S1
BA1	2 × CSEM	61 μm, 12 cm, $<100>$ 2.5 kΩ cm	-	1 × APV25S1
BA2	2 × CSEM	61 μm, 12 cm, $<111>$ 6 kΩ cm	10^{14}	1 × APV25S1
PD27	2 × Micron	61 μm, 12 cm, $<100>$ 2 kΩ cm, OX	10^{14}	1 × APV25S1
VB25	2 × Hamamatsu	140 μm, 12 cm, $<100>$ 6 kΩ cm	-	3 × APV25S0
PD1	2 × Micron	61 μm, 12 cm, $<100>$ 6 kΩ cm	-	2 × APV6
PD4	2 × Micron	61 μm, 12 cm, $<100>$ 1.4 kΩ cm	$2 \cdot 10^{14}$	2 × APV6

The silicon wafers of n-type and a thickness of 300 μm were processed by Micron and CSEM with p+ strips which are $\sim$ 18 μm wide, 60 mm long and have a 61 μm pitch. Larger sensors were produced at Hamamatsu on 320 μm thick wafers with 35 μm wide, 80 mm long strips and 140 μm pitch.

All sensors were AC coupled and the bias was delivered through $\sim$ 2 MΩ polysilicon resistors.

The wafers had different crystal orientations $<111>$ or $<100>$ and a bulk resistivity between from 1.4 and 7 kΩ cm. Some sensors were produced using the oxygenation (OX) technique which allows a reduction of the operating voltage for sensors irradiated with charged particles [2]. The oxygenation was performed from a local oxygen layer grown into the bulk at 1200° C during 100 hours, resulting in an oxygen concentration of about $3 \cdot 10^{17}\,\mathrm{cm^{-3}}$. Selected detectors were pre-irradiated by 25 ... 34 MeV protons to an equivalent fluence of $1 \ldots 2 \cdot 10^{14}$ n(1MeV)/cm^2. Typical IV curves for different sensors are presented in figure 1.

2.2 Readout chips

Two successive generations of the APV chip were used to read out the sensors: APV6 and APV25 (both S0 and S1 versions). While the APV6 chip is manufactured in a 1.2 μm radiation hard CMOS process, the newer APV25 is made in commercial 0.25 μm deep sub-micron CMOS, which provides intrinsic radiation tolerance. With the APV25 redesign, several improvements were implemented and new features were added to the chip.

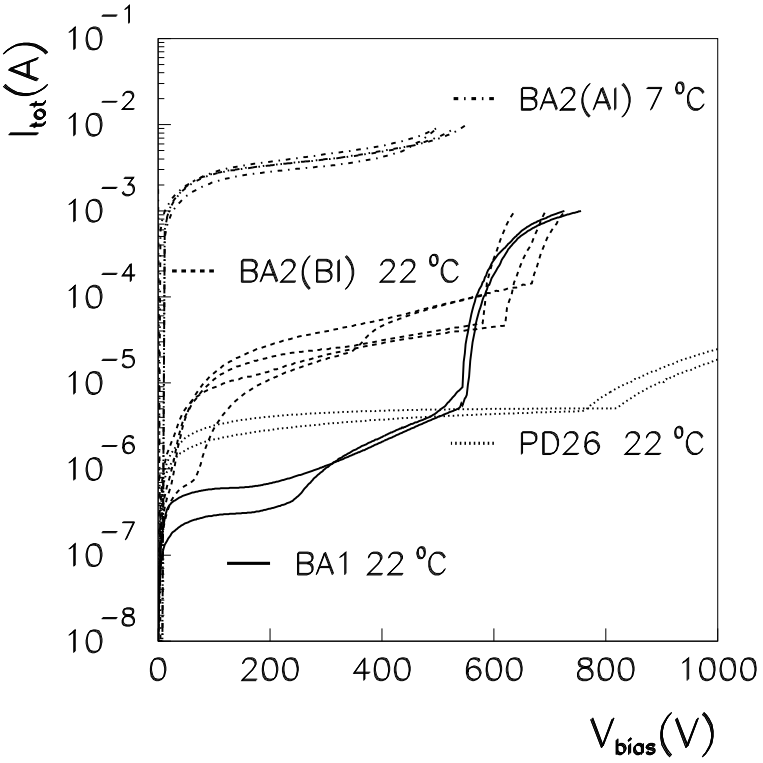

Figure 1: Typical IV curves for different sensors before (BI) and after (AI) irradiation.

The APV chip consists of 128 analog channels, each consisting of a preamplifier followed by a CR-RC shaper with a time constant of $\tau = 50\,\text{ns}$. The shaper output is sampled at 40 MHz and stored in an analog pipeline of 160 (APV6) or 192 (APV25) cells. This front-end buffer is required by the first-level trigger latency, which will only arrive about $3\,\mu\text{s}$ after the respective bunch crossing. The APV chips are equipped with an I^2C interface for slow controls such as bias settings and a fast, synchronous trigger input.

When a trigger arrives at the APV, three consecutive samples are processed by a switched capacitor filter which performs a deconvolution algorithm [3] that effectively narrows each pulse down to one single clock cycle in order to identify the exact bunch crossing from which the observed particle originates. Alternatively, this deconvolution filter can be switched off which results in "peak mode" operation. Since the "deconvolution mode" is the default operating condition in CMS, most of our measurements were performed in this mode.

The "multi-peak mode" of the APV25 chip allows to visualize the pulse shape of particle signals by sending a set of consecutive triggers around each pulse (fig. 2). Moreover, the shaping curve can also be obtained using the internal calibration circuit.

The predominant noise source in the detector and readout system is the front-end amplifier and its preamplifier input transistor in particular. The measured noise [4] of APV6 and APV25 are shown for both peak and deconvolution modes in table 2.

Table 2:

Chip	ENC_{peak} [e]	ENC_{dec} [e]
APV6	$510 + 36\,\text{pF}^{-1}$	$1000 + 46\,\text{pF}^{-1}$
APV25	$250 + 36\,\text{pF}^{-1}$	$400 + 60\,\text{pF}^{-1}$

Other noise contributions such as leakage current, strip resistance or bias resistor together only account for about $430\,\text{e}^-$ which is quadratically added [1]. With a capacitive load of 16 pF, which is typical for CMS detectors, we expect ENC = $1426\,\text{e}^-$ with the APV25 in deconvolution mode, which is in good

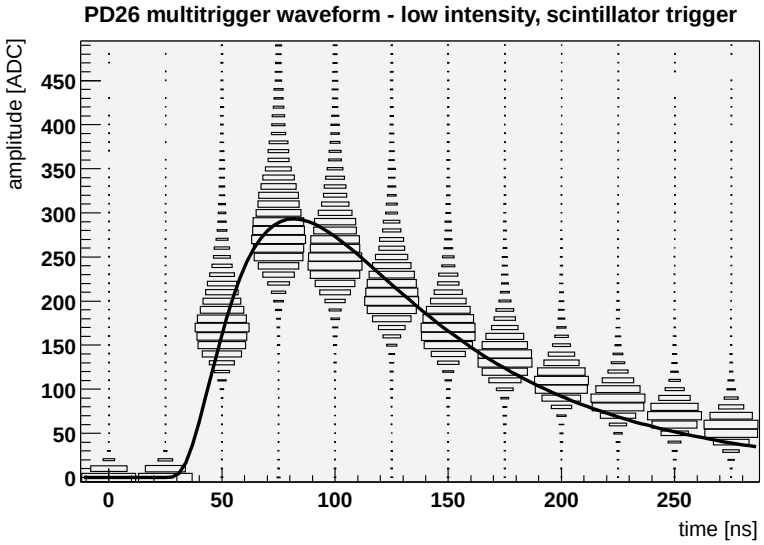

Figure 2: The averaged shaper output waveform, measured with 350Mev/c pions in multitrigger mode.

agreement with the measured value of $1430\,e^-$.

One to three readout chips (see table 1) were mounted on hybrids developed at HEPHY (Vienna) and INFN (Padova). The hybrid was assembled with a pitch adapter on the detector frame carrying two daisy-chained sensors.

3 Experimental setup

All detector modules under study were housed in a cooling box which was operated by two water cooled peltier elements with a total cooling power of $\sim 200\,W$ at $\Delta T \sim 40°\,C$ ($T_{box} = -20°\,C$). The box was flushed with dry nitrogen at a refresh rate of ~ 0.3 renewals/hour to prevent water condensation.

The tests were performed in the PSI πM1 beam line which provides 350 MeV/c pions or protons with a rate of up to $9\,kHz/mm^2$ and a beam spot of approximately $50 \times 50\,mm^2$ FWHM. In the present study we operated the detectors mostly with pions at a rate of $100\,Hz/mm^2$. Although 350 MeV/c pions are approximately minimum ionizing particles (MIPS), secondary reactions can produce heavily ionizing particles (HIPS) with up to 1000 times larger ionization losses.

3.1 DAQ

The data acquisition system was designed at HEPHY and consists of several dedicated VME modules in the back-end and local voltage regulators and buffer amplifiers in the front-end [6]. The APVs are controlled by a custom-made VME sequencer board which can operate in two different modes: either incoming triggers are delayed by a shift register of adjustable length or one of four programmable trigger sequences (or a combination of them) is sent to the APVs after receiving an activation input. In either mode, triggers can be received from an external source or generated by software. The first mode is typically used with a scintillator trigger, while the latter is used for pedestal evaluation and calibration runs.

The 40 MHz APV clock is derived from the 50 MHz PSI clock using a custom PLL-based circuit, which features phase stability between the two clocks and returns a synchronization pulse when both clocks are in phase, which occurs with a period of 100 ns. This SYNC pulse is used to select particles which are in phase with both clocks. A scintillator of $12 \times 12\,mm^2$ was placed behind the detector modules and read out by two photomultipliers equipped with a preamplifier, allowing operation at relatively low bias voltage to prevent pileup at high beam intensity.

Opto-coupled VME $-$ I^2C modules with a bus extender took care of the APV slow control. The analog chip output was digitized by custom 40 MS/s ADCs with 12 bit resolution. Usually data were transferred between the beam area and the counting room by twisted pair copper cables of 25 m length, but in the

analog path, a prototype of the optical link was also successfully tested which performed similar to the copper cable.

The data acquisition was run under the CVI development system on a Windows PC. It allowed different modes of operation (normal, pedestal, calibration runs) and offered a wide range of online analysis capabilities. A second PC was used for the slow control and monitoring of the cooling box and the detector bias voltages.

4 Results

4.1 Front-end electronics

Irradiation may cause two kinds of damages to the readout electronics: permanent or transient.

Due to its deep sub-micron fabrication process, the APV25 should be intrinsically radiation tolerant, which was verified in a dedicated test at the PSI with eight APV25S1 chips which were irradiated to $1.87 \cdot 10^{14}\pi/cm^2$ at 300 MeV/c momentum [5]. All chips were in operation and continuously read out during the irradiation [6]. No critical, irreversible damage (such as a Single Event Gate Rupture or Latchup) was observed. The irradiation did not affect the calibration signal SNR within $\pm 5\%$. We have observed a dependance of the calibration SNR on the temperature of about $\sim 25\%$ for ΔT=30^{o}C. This dependance was expected and is due to variation of the chip settings which have to be optimized for each temperature.

The charge released by HIPS can result in the flipping of an APV register cell, called a Single Event Upset (SEU). Then, the chip internal state machine is disturbed and the data output may be corrupted until a reset signal is sent to the APV, which restores initial conditions. We measured a total cross section of approximately $2 \cdot 10^{-12} cm^2$ for such digital SEU, corresponding to $2 \cdot 10^{-15} cm^2$ for a single flip-flop cell. From extrapolation of these data, a total upset rate in the order of 100 SEUs/hour is expected for the Inner or Outer Barrel parts of the CMS Tracker. Single event upsets also occur in the analog circuitry, but are self-repairing and appear as a negligible increase in noise background. Details of the SEU study can be found in [5] and [6].

In order to test the uniformity of the APV gain map for all channels and pipeline addresses the latency has been varied. We did not observe any change in the signal for different pipeline addresses. A variation of the calibration signal below 5% has been observed across the chip except for the non bonded strips which revealed larger amplitudes due to the missing capacitive load.

4.2 Detector behavior

4.2.1 Data analysis

The data analysis is based on the ORCA v.3 package [7]. This can be subdivided into two parts, pedestal evaluation and clustering algorithm. During the pedestal calculation an rms noise (σ) for each channel is estimated, while the clustering algorithm selects signals above thresholds determined by the rms values. In CMS it is foreseen that the rms values are estimated in a special calibration run when all APV channel data are transferred to the Front-End Driver (FED) crate controller where the data are analyzed [8]. Afterwards the calculated thresholds are loaded into the FED memory and only the cluster information is sent to the computer farm during physics runs.

- Pedestal algorithm. We consider two different scenarios for pedestal and rms noise evaluations.

  1. The noise is estimated during the calibration run with limited statistics. At PSI, the first 600 events in each run were produced with a random software trigger and have been used for the calibration.
  2. The TDR procedure [1] updates pedestal and rms during the whole run [9].

  For both methods the noisy channels or the channels with hits are suppressed if the updated $\mathrm{SNR}_i = \frac{signal(i)}{\sigma(i)} > \mathrm{T}_{ped}$, where signal_i=(data_i-$\mathrm{pedestal}_i$-common mode noise_i). The threshold $\mathrm{T_{ped}} = 3$ was chosen to get the statistical rms closer to the value obtained by the Gaussian fit, see figure 3.

The common mode noise was calculated by a mean algorithm with 3 iterations and with a weighted mean calculation [9]. The weight for each channel was set proportional to $(1/\sigma)^2$.

- Clustering algorithm. Two different algorithms have been used:

  1. The FED2 algorithm selects channels with SNR>5 and the channels with SNR>2 if the cluster size (clsz) is above 1. For the common mode subtraction a median algorithm has been used [8]. We have used the first scenario for the noise evaluation together with the FED2 algorithm. These algorithms can be implemented in the final electronics.
  2. The TDR algorithm. The cluster was created from a seed strip with SNR > 3 and neighbors with SNR > 2. The iterative mean algorithm for the common mode subtraction was used.

  The cluster SNR_{clus} defined as $\frac{Q_{cluster}}{\sqrt{\sum_{clsz} rms_i^2}}$ should be above 5 for both methods. No holes are allowed in the cluster.

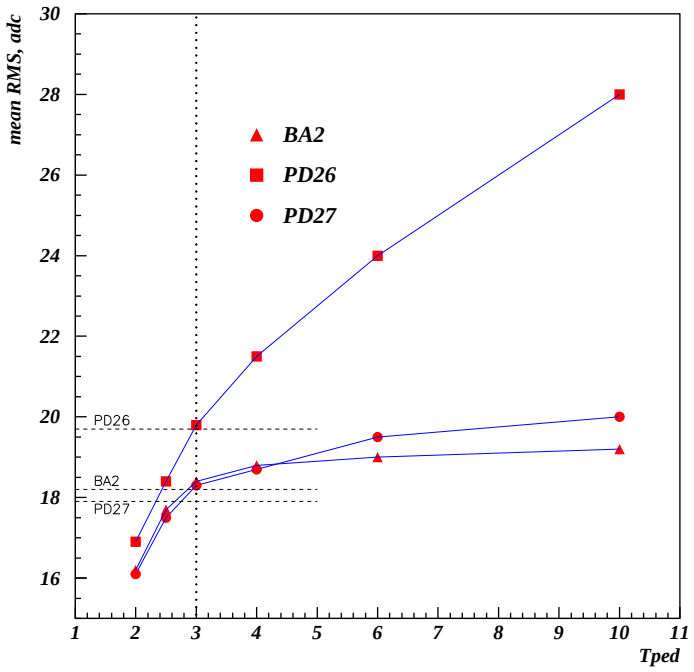

Figure 3: Averaged rms noise in deconvolution mode obtained with different thresholds $\mathrm{T_{ped}}$ for noisy/hit channels suppression. The dashed lines show the values obtained by the Gaussian fit.

In the presence of a large common mode noise, noisy channels or particle hits, the calculated rms value depends on the statistics. In figure 4 the evolution of the averaged rms is presented for different modules. Note that at higher particle rate the rms noise can be overestimated when using the same threshold.

The common mode fluctuations depend on the experimental setup and can be higher than the intrinsic APV noise. At PSI, the typical common mode noise was about twice as high as the uncorrelated noise. The channels which are not bonded to the sensor, or less sensitive to the noise due to the detector layout, are less prone to these fluctuations and after the common mode subtraction themselves appear as 'noisy' channels. The common mode subtraction algorithm masks these channels as well as truly noisy channels if $\mathrm{SNR}_i > \mathrm{T_{ped}} = 3$. Moreover, channels with $\mathrm{rms}_i^2 > \mathrm{T_{ped}} \times (\mathrm{averagechiprms})^2$ were masked too. At average, each chip had about six masked channels in our tests. We found that the common mode offset was not perfectly uniform across the chip as shown in figure 5. Moreover, the remaining uncorrelated noise was depending on the grouping of channels during the common mode subtraction, where the best results were obtained with groups of 16 or 32 channels (figure 6).

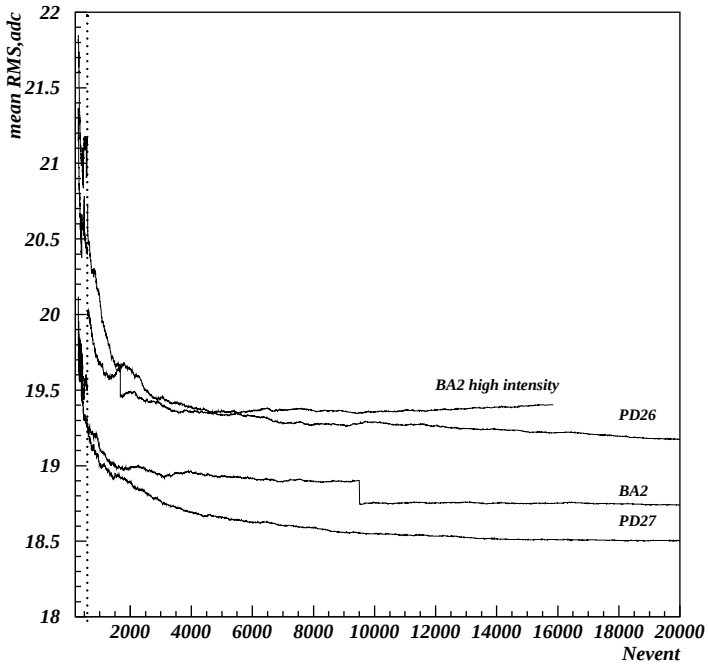

Figure 4: The evolution of the averaged rms noise in the TDR scenario at a rate of $\sim 100\,\mathrm{Hz/mm^2}$. The steps in the rms of the BA2 and PD26 detectors correspond to the masking of new 'noisy' strips. Same evolution at higher rate ($4.5\,\mathrm{kHz/mm^2}$) is shown.

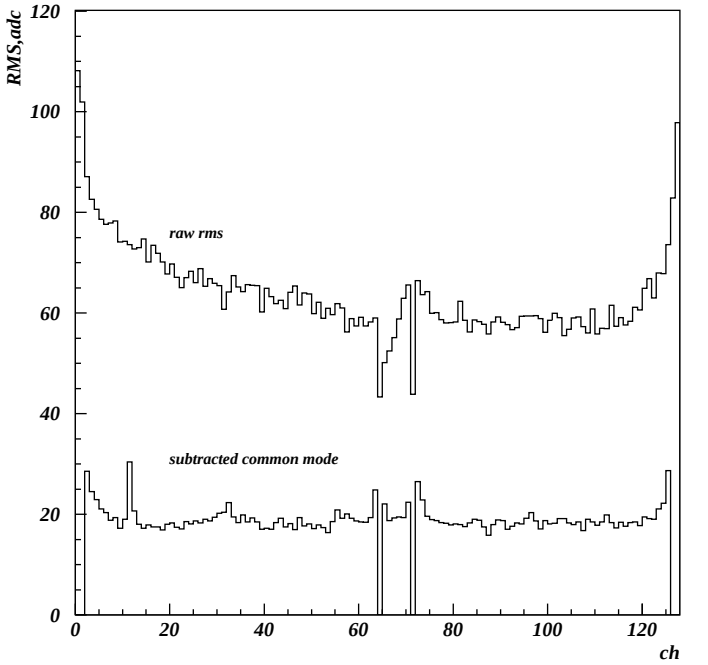

Figure 5: Rms noise before and after common mode subtraction of the PD27 detector read out by one APV25 chip.

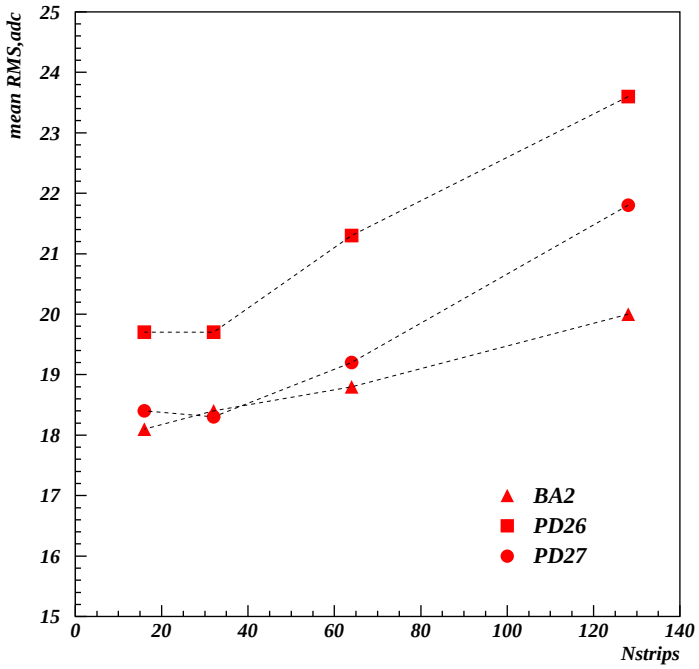

Figure 6: Dependence of the intrinsic rms noise on the number of strips in the common mode group (16, 32, 64, 128).

Typical signal-to-noise distributions obtained with FED2 and TDR clustering algorithms are presented in figure 7. The FED2 algorithm has a lower threshold for wider clusters and should provide better efficiency in comparison with the TDR algorithm at the price of somewhat higher occupancy. Note that the sensitivity of the algorithms to the cluster size may require an individual tuning of thresholds for a particular detector type.

4.2.2 Signal-to-noise performance

The SNR was analyzed from runs collected in the 350 MeV/c pion beam, at a rate below 100Hz/mm^2, with the readout electronics operated in deconvolution mode. For each detector we select events with one cluster only, which is about 70% of full statistics.

Figure 8 shows that the averaged rms noise is almost independent from the bias voltage. Only for the BA2 detector module the noise was slightly lower at higher voltages, which we account to a heavier dependence of the inter-strip capacitance on V_{bias} for sensors with $< 111 >$ crystal orientation.

Figures 9 and 10 present the most probable (MP) SNR_{clus} values calculated according to the FED2 algorithm as a function of V_{bias}. Note that all irradiated detector modules have shown stable operation at a bias voltage of 550 V. The highest SNR of about 16.5 was achieved with the non-irradiated PD26 detector. As expected, the APV25 readout provides an ~30% increase of the SNR due to lower noise compared to the APV6. Even irradiated detectors reveal a SNR above 12 when read out by the APV25 chip. The significant difference in the signal obtained for the irradiated detectors BA2 and PD27, both equipped with the APV25 chip, can be explained by different production technologies. The BA2 was produced with $< 111 >$ crystal orientation, while the PD27 was manufactured from $< 100 >$ silicon using the oxygenation technique [10]. The irradiated oxygenated sensor (PD27) demonstrated almost the same SNR as the non-irradiated (PD26) at $V_{bias} = 550$ V while the non-oxygenated irradiated sensor (BA2) had lost $\sim 20\%$ of the signal in comparison with the non-irradiated one (BA1). In table 3 we summarize the maximum SNR_{clus} values obtained for each detector. For the irradiated sensors the maximum SNR was achieved at V_{bias} ~3 times above the expected $V_{depletion}$.

The cluster size (figure 11) is larger for irradiated detectors presumably due to an under-depleted zone near

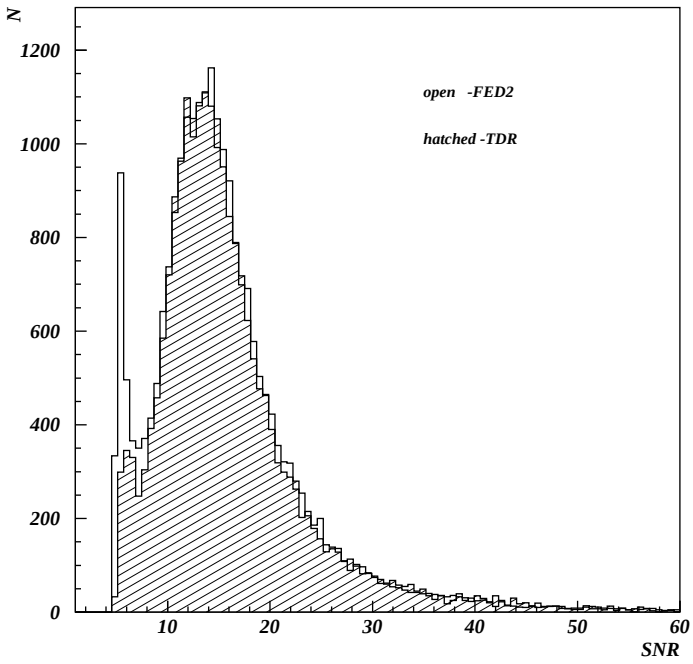

Figure 7: SNR distributions in deconvolution mode obtained with FED2 (open) and TDR (hatched) algorithms for the PD27 detector.

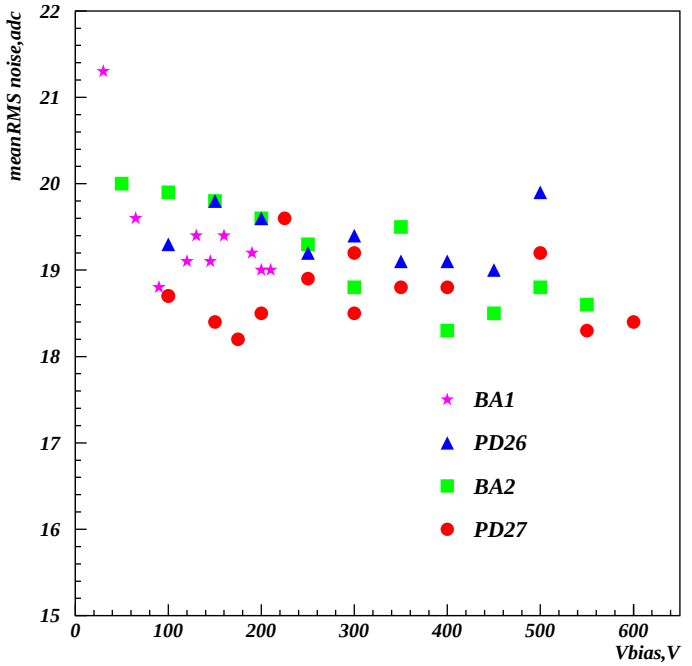

Figure 8: Mean rms noise versus V_{bias} at $T = -10°$ C (BA1 at $T = 18°$ C) for detectors read out by the APV25 chip in deconvolution mode.

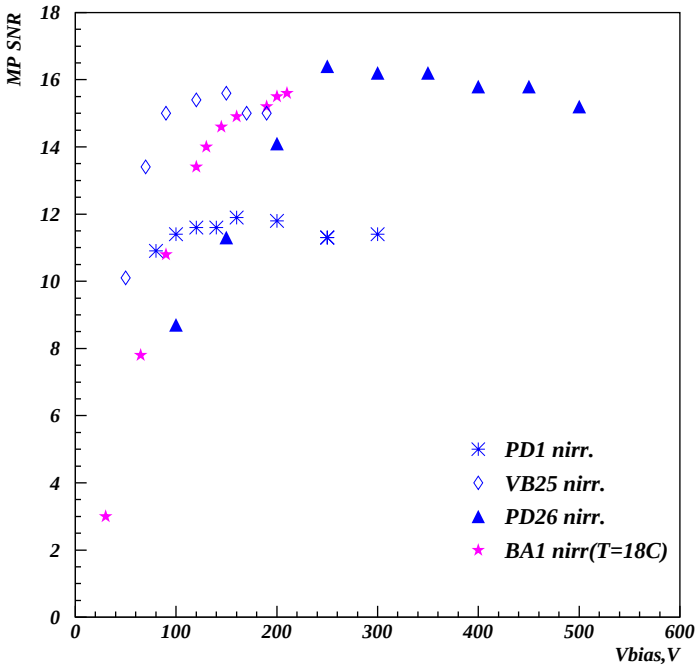

Figure 9: SNR in deconvolution mode versus V_bias for non-irradiated detectors read out by APV25 (VB25, PD26, BA1) and APV6 (PD1) chips at $T = -10°$ C (except BA1).

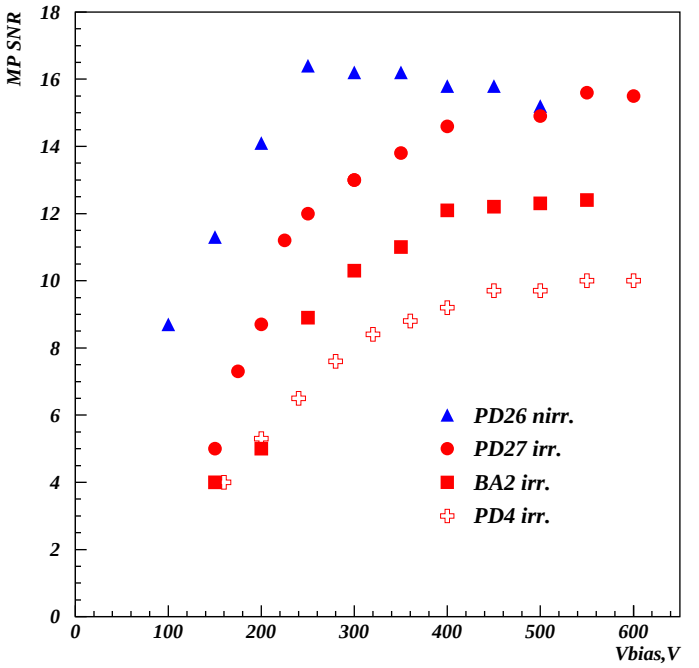

Figure 10: SNR in deconvolution mode versus V_{bias} for irradiated and non-irradiated detectors ($T = -10°$ C).

Table 3:

detector	specification	SNR_{max}	V_{bias},V
PD26	nirr, < 100 >, APV25S1, OX	16.5	250
BA1	nirr, < 100 >, APV25S1	15.5	200
BA2	irr, < 111 >, APV25S1	12.5	550
PD27	irr, < 100 >, APV25S1, OX	15.5	550
VB25	nirr, < 100 >, APV25S0	16.0	150
PD1	nirr, < 100 >, APV6	12.0	200
PD4	irr, < 100 >, APV6	10.0	550

the p+ strips and charge trapping. The dependence of the cluster size on V_{bias} follows the dependence of the interstrip capacitance C_{int}. For irradiated sensors, C_{int} decreases with V_{bias}, especially for the < 111 > crystals, while for non-irradiated sensors, C_{int} remains constant and for irradiated < 100 > crystals, the dependence on V_{bias} is weaker.

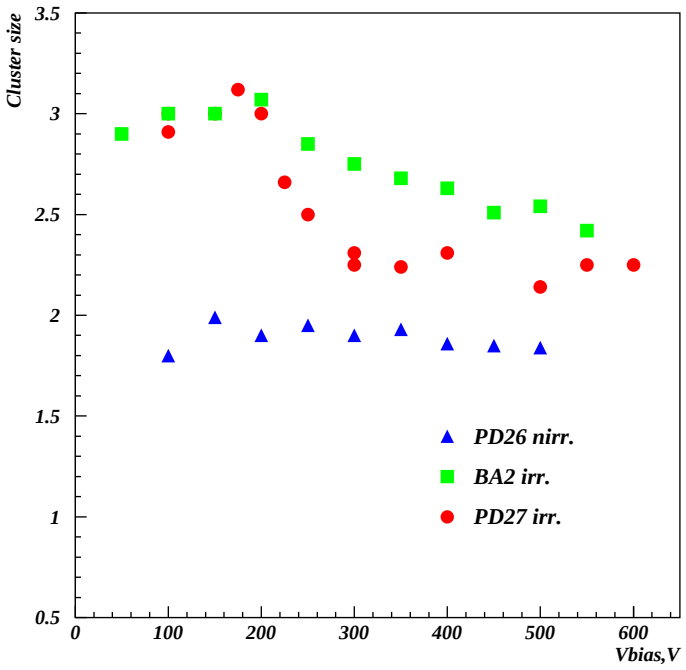

Figure 11: Cluster size versus V_{bias} in deconvolution mode.

Due to the absence of precise independent tracking and large multiple scattering we could not measure the absolute efficiency. However we can roughly estimate the knee of the efficiency plateau by using the detectors under test as a tracker. In figure 12 the efficiency versus SNR calculated by the FED2 and the TDR algorithms is shown for the irradiated BA2 detector. The tracks were reconstructed by the PD27(front) and PD26(back) detectors. The efficiency plateau starts at SNR~8 using the FED2 algorithm.

To study the SNR uniformity the beam spot has been moved along the strips. No variation in the SNR has been found for the largest VB25 detector in a beam spot scan from one end to the opposite end. The measured variation of the SNR across the sensor was below 2.5% for all detectors.

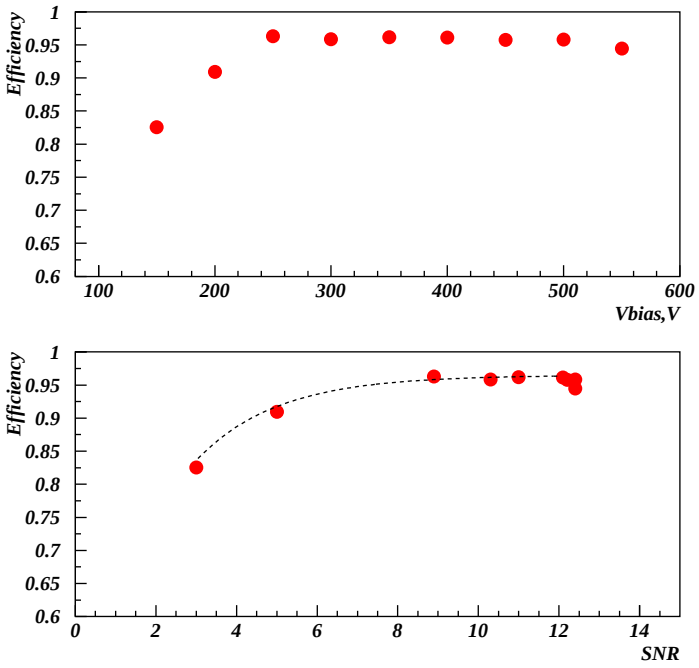

Figure 12: Efficiency versus V_{bias} and MP SNR for the BA2 detector operated at $T = -10°$ C in deconvolution mode.

4.2.3 Angular dependence

Unlike our measurements at PSI, where the beam incidence was usually perpendicular to the detector plane, a wide-spread angular distribution is expected in CMS [1]. An incident angle scan was performed with the 140 μm pitched VB25 module at room temperature to test the detector behavior. In figure 13 the most probable signals and the cluster sizes are presented versus the incident angle α to the detector plane for pion and proton beams at a momentum of 350 MeV/c. The signal dependence is described with $1/cos(\alpha)$ and the cluster size with $\sqrt{c^2 + tan^2(\alpha)}$ functions, where c denotes the cluster width at perpendicular incidence.

The ratio of $\frac{SNR_p}{SNR_\pi}$ is about 6.6 and thus in good agreement with the calculation from the restricted Bethe-Bloch theory which predicts 6.0.

5 Summary

Several CMS silicon strip detector modules equipped with both APV6 and APV25 readout chips were tested in a pion/proton beam under conditions close to what is expected at the LHC. The APV25 chip, which is manufactured in the 0.25 μm deep submicron process, has a significantly lower noise level than its predecessor. With a strip length of 12 cm and irradiated sensors, we obtained signal-to-noise value of 15.5 for the APV25 and 10 for the APV6 chips in deconvolution mode. The signal-to-noise is uniform along and across the strips within a level of 5%.

The signal-to-noise of sensors equipped with APV25 readout is high enough to assure efficient operation even after ten years of LHC with a considerable safety margin. The absolute value of the SNR depends on the analyzing algorithm which has to be optimized according to the expected conditions.

It has been shown that the sensors and the readout chips do survive in the harsh radiation environment of CMS. No critical damage could be observed on the readout chips, and the single event upset rates are sufficiently low so they will cause only negligible corruption of data.

In an angle scan, the detector modules behaved as expected from geometrical relations and the measured signals were consistent with the restricted Bethe-Bloch theory for pions and protons.

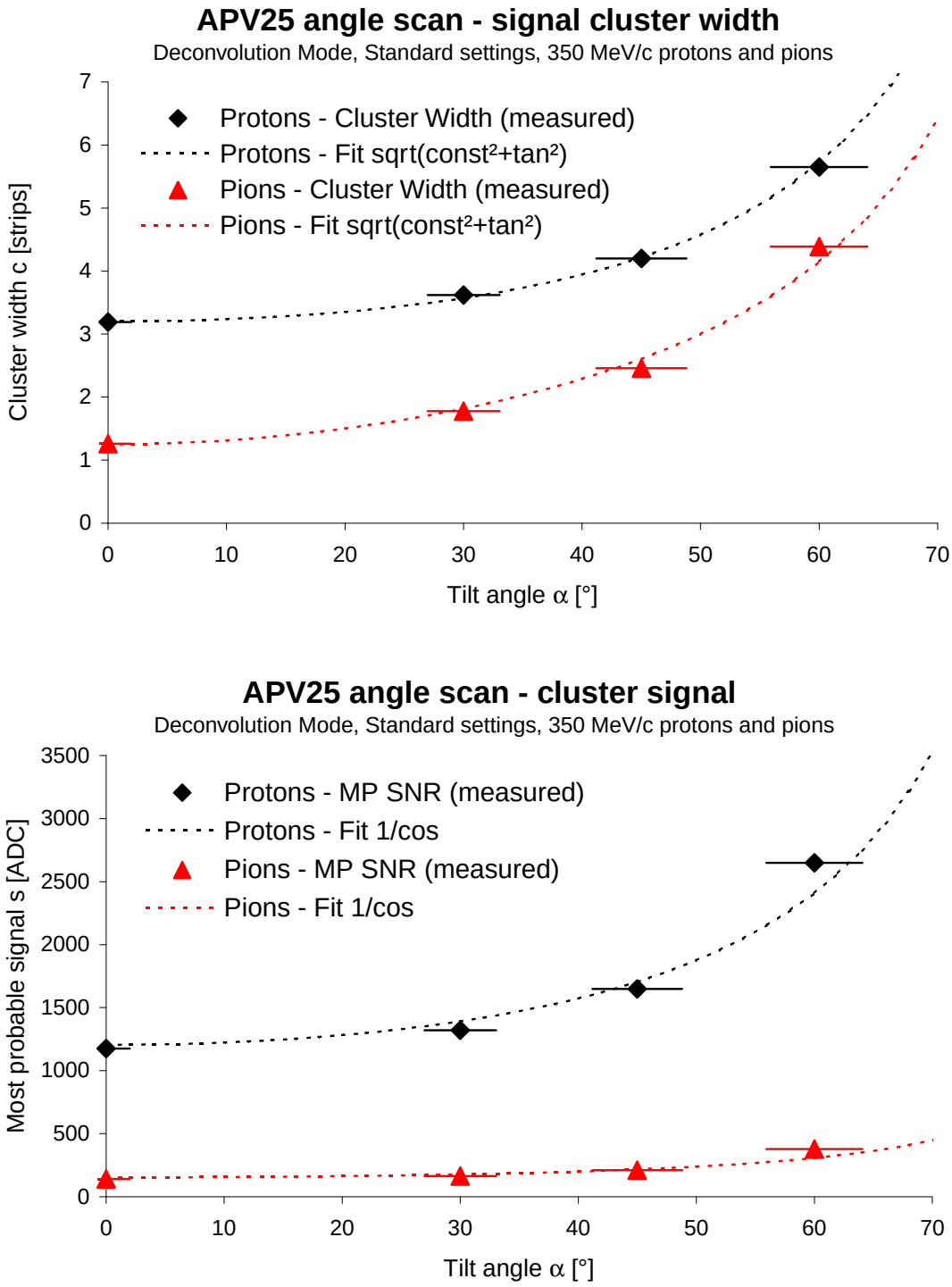

Figure 13: Cluster size (top) and most probable signal (bottom) of the VB25 detector module versus incident angle for 350 MeV/c pion and proton beams in deconvolution mode.

The electronic readout chain was successfully operated both with a copper cable transmission and with a prototype of the analog optical link.

6 Acknowledgments

We would like to thank K.Gabathuler and D.Renker for their help at PSI and L.Shektman for sharing the beamline with us.

References

[1] CMS Tracker Technical Design Report, CERN/LHCC 98-6, 1998.

[2] A.Ruzin for RD48, NIM A 447 (2000), 116.

[3] S.Gadomski et al., NIM A 320 (1992), 217-227

[4] M.French, APV User Manuals, http://www.te.rl.ac.uk/med.

[5] M.Friedl et al., Proceedings of the Vertex 2001 conference (to be published in NIM A).

[6] M.Friedl, Dissertation, Vienna 2001, http://cern.ch/friedl.

[7] ORCA CMS, http://cmsdoc.cern.ch/ORCA.

[8] I.Tomalin. CMS-IN 2001/025. http://cern.ch/tomalini/.

[9] S.Braibant et al. CMS NOTE 2000/050.

[10] N.Demaria et al., NIM A 447 (2000) 142-150.